DiVA
http://www.diva-portal.org

Preprint

This is the submitted version of a paper published in *Applied Optics*.

Citation for the original published paper (version of record):

Khodadad, D. (2025)
Fast and accurate phase unwrapping for complex phase maps
Applied Optics, 64(24): 6910-6910
https://doi.org/10.1364/ao.567228

Access to the published version may require subscription.

N.B. When citing this work, cite the original published paper.

Permanent link to this version:
http://urn.kb.se/resolve?urn=urn:nbn:se:umu:diva-243941

Fast and accurate phase unwrapping for complex phase maps

DAVOOD KHODADAD

Department of Applied Physics and Electronics, Umeå University, 90187, Umeå, Sweden
davood.khodadad@umu.se

Received XX Month XXXX; revised XX Month, XXXX; accepted XX Month XXXX; posted XX Month XXXX (Doc. ID XXXXX); published XX Month XXXX

Phase unwrapping is fundamental in interferometric data analysis but remains challenging in the presence of discontinuities and complex structures. In this paper, a new, fast, and robust phase unwrapping technique is introduced. The method segments the wrapped phase based on gradient polarity, ensuring that each region contains phase gradients in only one direction. By eliminating reversing or conflicting gradients within each segment, the approach reduces complexity, making unwrapping more efficient and less error-prone. Each segmented region is then independently unwrapped, simplifying the process and minimizing error propagation. After unwrapping, the segments are merged to reconstruct a globally consistent phase map while preserving true phase discontinuities from the original data. The method enhances computational efficiency while maintaining high accuracy. The proposed approach was evaluated using both simulated and experimental datasets involving challenging phase structures, such as spiral shear phase maps, and was found to consistently outperform conventional algorithms. This framework offers a scalable solution for applications in optical metrology, SAR imaging, and medical diagnostics.

1. Introduction

Phase unwrapping is a critical and challenging task in interferometric data analysis, where the goal is to recover the true (absolute) phase from its wrapped representation, typically modulo 2π. This problem arises in a wide range of coherent imaging and measurement techniques, including optical interferometry (OI), magnetic resonance imaging (MRI), fringe projection profilometry (FPP), and interferometric synthetic aperture radar (InSAR). In these applications, the absolute phase is directly proportional to important physical quantities such as thickness or refractive index in OI, magnetic susceptibility or flow velocity in MRI, 3D surface profile and deformation of objects in FPP, and surface displacement or topography in InSAR. Thus, reliable phase unwrapping is essential to retrieve meaningful physical data from the raw measurements.

The wrapped phase in these techniques is typically computed using the arctangent of the complex amplitude field, which inherently restricts the result to the principal value range of $(-\pi, \pi]$. However, in most real-world scenarios, the true underlying phase exceeds this limited range. As a result, to retrieve the actual physical quantity of interest, the initial wrapped phase must be transformed into a continuous absolute phase map through phase unwrapping. This step although straightforward in the case of smooth, noise-free, and continuous phase fields, becomes significantly more complex when the data include noise, abrupt phase discontinuities, or complex spatial structures with sudden phase changes [1-7].

Various techniques have been developed to reduce phase ambiguity or extend the unwrapping range prior to reconstruction, such as multi-wavelength methods [8, 9], multi-directional illumination [10-12], and approaches that bypass phase synthesis [13] or optimize unwrapping via phase correlation across wavelengths [14]. Additional strategies leverage complementary information, such as speckle displacement analysis [11, 15] or regularization-based priors [16]. However, despite these efforts, such methods remain constrained by system complexity, noise sensitivity, or limited scalability, and phase unwrapping continues to be a critical step in many practical, especially single-wavelength applications.

Even a single error in the unwrapping process can propagate throughout the entire phase map, severely compromising the accuracy of the final result. This issue becomes especially pronounced in complex phase structures (e.g., Figure 1 and 2) such as spiral shear phase maps where abrupt variations and directional inconsistencies challenge the assumptions of many conventional algorithms [1, 17].

Over the past four decades, the task of reconstructing a continuous phase field from its wrapped counterpart has driven extensive research, resulting in a wide variety of unwrapping algorithms. Each of these approaches is designed to address specific challenges such as noise suppression, discontinuity handling, or computational efficiency but none are universally optimal, and each comes with its own limitations [1, 2, 6, 18].

For example, while well-known techniques like the Itoh algorithm [19], the 2D-SRNCP method [20], the PUMA algorithm [21] and the TIE-based method [22] are effective unwrapping methods, they are unable to accurately unwrap more intricate structures like spiral shear phase maps. On the other hand, more sophisticated methods, such as the Flynn algorithm [23] and the weighted Lp-norm algorithm [24], can achieve high accuracy in these challenging cases, but at the

cost of significantly increased computational complexity, which restricts their practical applicability [1].

This highlights a critical gap in the field: the need for a method that is not only robust and accurate but also computationally efficient. In this paper, we address this gap by introducing a novel, robust and fast phase unwrapping strategy that leverages the intrinsic properties of phase gradient orientation (polarity). Our approach involves segmenting the wrapped phase map into regions based on consistent phase gradient polarity along both the X and Y axes. By partitioning the complex map into subregions with coherent directional behavior, we reduce the unwrapping complexity and isolate potential discontinuities or conflicts (reversing phase gradients).

This segmentation facilitates straightforward independent unwrapping within each region. Each segment is then unwrapped independently using a simplified procedure appropriate for its specific gradient characteristics. After unwrapping all segments, they are seamlessly merged to reconstruct the full continuous phase map. While this approach is specifically designed to handle complex phase structures with high accuracy and efficiency, it is equally effective for simpler phase maps.

This strategy not only simplifies the unwrapping process but also significantly enhances computational efficiency, making it highly suitable for both high-precision and real-time applications. Unlike existing methods that may suffer from propagation errors or intensive resource demands, our proposed technique emphasizes a balance between accuracy and efficiency. By taking advantage of structural regularities in the phase gradient and avoiding global unwrapping constraints, the algorithm proves effective even in complex cases where traditional methods fail.

2. Theoretical Foundation and Methodology

To obtain the true (absolute) phase φ, it must be estimated from the initially measured wrapped phase ϕ in a process known as phase unwrapping. The relationship between the wrapped and absolute phases is given by:

$$\varphi(\boldsymbol{r}) = \phi(\boldsymbol{r}) + 2\pi k(\boldsymbol{r}), \tag{1}$$

where $\boldsymbol{r}$ denotes the spatial coordinate along the wrapping direction, and $k(\mathbf{r}) \in \mathrm{Z}$ is the integer number of wraps.

Although this estimation seems straightforward, the phase unwrapping problem is inherently ill-posed, as both φ and k are unknown. However, if the absolute phase φ is continuous and free of discontinuities, the problem becomes well-posed, and the gradients of φ and ϕ satisfy:

$$\nabla\varphi = \Upsilon(\nabla\phi) = \begin{cases} \nabla\phi, & |\nabla\phi| \le \pi \\ \nabla\phi - 2\pi, & \nabla\phi > \pi \\ \nabla\phi + 2\pi, & \nabla\phi < -\pi \end{cases}, \tag{2}$$

where $\Upsilon(\cdot)$ is the unwrapping operator that eliminates multiples of 2π, keeping the result within the principal interval $(-\pi, \pi]$ and ∇ denotes the gradient (central difference) operator.

Using this relationship, the absolute phase φ at a point $\mathbf{r}_1$ can be computed by integrating the corrected phase gradient along a path L from a reference point $\mathbf{r}_0$:

$$\varphi(\boldsymbol{r}_1) = \varphi(\boldsymbol{r}_0) + \int_L \nabla\varphi d\boldsymbol{r} = \varphi(\boldsymbol{r}_0) + \int_L \Upsilon(\nabla\phi) d\boldsymbol{r}. \tag{3}$$

In two-dimensional scenarios, this expression becomes:

$$\varphi(x,y) = \varphi(x_0,y_0) + \int_C \left[\Upsilon\left(\frac{\partial\phi(x,y)}{\partial x}\right)dx + \Upsilon\left(\frac{\partial\phi(x,y)}{\partial y}\right)dy\right], \tag{4}$$

where C is any path within the wrapped phase map connecting the reference point (x_0, y_0) to the evaluation point (x, y).

The unwrapping process begins with Eq. (4). Given a wrapped phase image $\phi(x, y)$, local phase variations can be analyzed and independently unwrapped using finite-difference approximations of the first-order gradients in the horizontal (X-axis) and vertical (Y-axis) directions:

$$G_x(x,y) = \frac{\partial\phi(x,y)}{\partial x}$$
$$G_y(x,y) = \frac{\partial\phi(x,y)}{\partial y} \tag{5}$$

Here, $G_x(x, y)$ and $G_y(x, y)$ represent the wrapped phase gradients along the X and Y directions, in Eq. (4), respectively. These gradient maps help assess phase continuity and identify locations of wrapping-induced discontinuities.

To demonstrate the practical implementation of this formulation, the unwrapping procedure is applied step by step to two wrapped phase distributions derived from an original surface dataset (distributed with [1]). This structured example-based approach provides a clear illustration of how the gradient components $G_x(x, y)$ and $G_y(x, y)$ are employed in the reconstruction of the absolute phase $\varphi(x, y)$, thereby highlighting the effectiveness and applicability of the proposed method in resolving phase discontinuities.

Figure 1(a) shows the first wrapped phase distribution $\phi(x, y)$, consisting of two adjoining surface regions with opposing slopes, one with a positive gradient and the other with a negative gradient. This configuration induces abrupt transitions in phase direction and presents a challenge for conventional unwrapping techniques, which often fail in the presence of such conflicting local gradients. The corresponding 3D surface representation is shown in Figure 1(b).

Figure 2(a) presents the second test case, also derived from the dataset in [1], comprising two intertwined spiral structures constructed on two sheared planes. The corresponding 3D surface representation of this phase map is depicted in Figure 2 (b). As seen in the figure, the phase surface contains multiple discontinuities and reversing phase variations, making it an extremely challenging phase unwrapping problem in the absence of prior information about the location

of these discontinuities [1, 21, 25]. This specific wrapped phase image serves as a demanding test case due to its intricate phase structure.

The proposed unwrapping methodology is developed and explained step by step through these two cases. At each stage—gradient analysis, segmentation, artifact suppression, local unwrapping, and final reconstruction—the corresponding intermediate results are presented. This case-driven formulation provides a clear and detailed illustration of the algorithm's logic and implementation in handling complex wrapped phase data.

Starting from the gradient formulation in Eq. (5), the unwrapping process proceeds by analyzing spatial variations in the wrapped phase through its horizontal and vertical gradients, $G_x(x,y)$ and $G_y(x,y)$, respectively. The horizontal gradient $G_x(x,y)$ in both cases (Figures 3a and 4a) reveals two distinct regions of opposing polarity—positive and negative phase gradients—while the vertical component $G_y(x,y)$ remains zero throughout the image (Figures 3b and 4b). The polarity of $G_x(x,y)$ is used as the basis for segmentation. The resulting gradient polarity-based

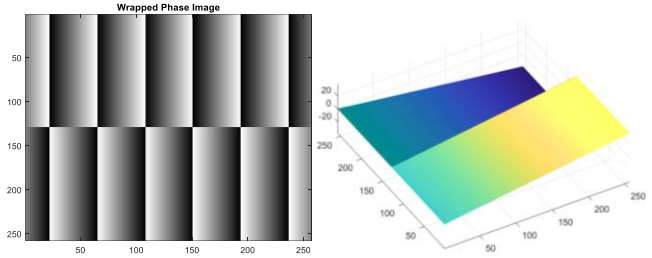

(a) (b)

Figure 1. (a) Wrapped phase image $\phi(x,y)$ with 257 × 257 pixels, composed of two adjacent surface regions with opposing phase gradients. The conflicting gradient directions, with a distinct boundary between the positive and negative slope regions, pose a significant challenge for conventional unwrapping methods. (b) Corresponding 3D surface representation of the wrapped phase map, illustrating the shear structure and sharp phase transition across the boundary.

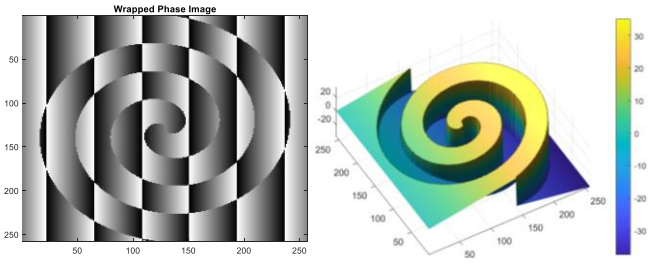

(a) (b)

Figure 2. (a) Wrapped phase image $\phi(x,y)$ with 257 × 257 pixels, containing two intertwined spirals constructed on two sheared planes. (b) Corresponding 3D surface representation of the wrapped phase map. The phase surface exhibits multiple discontinuities, making phase unwrapping highly challenging without prior knowledge of discontinuity locations.

segmentations are shown in Figures 3c and 3d for Case 1, and Figures 4c and 4d for Case 2. Figures 3c and 4c contain only zero or positive gradient pixels, while all other pixels are assigned NaN (Not a Number) values. Conversely, Figures 3d and 4d contain only negative gradient pixels, with all remaining pixels similarly masked as NaN.

To prevent large phase fluctuations in wrapping pixels from being misinterpreted as discontinuities or change of phase gradients, a tolerance-based filtering method is applied. A tolerance threshold τ is used to avoid misinterpretation of phase gradients due to the wrapping pixels. Positive phase gradients $G_x^+(x,y)$ regions correspond to areas where the phase is increasing. $G_x^+(x,y)$ is then defiend as:

$$G_x^+(x,y) = \begin{cases} G_x(x,y), & if\ G_x(x,y) \geq 0\ or\ G_x(x,y) \leq -\tau \\ NaN & otherwise \end{cases} \quad (6)$$

This ensures that only positive gradients are retained, while negative values are removed.

Negative phase gradients regions $G_x^-(x,y)$ in contrast correspond to areas where the phase is decreasing and is defined as:

$$G_x^-(x,y) = \begin{cases} G_x(x,y), & if\ G_x(x,y) < 0\ or\ G_x(x,y) \geq \tau \\ NaN & otherwise \end{cases} \quad (7)$$

where retains negative gradients while removing positive values.

After segmenting the regions of $G_x^+(x,y)$ and $G_x^-(x,y)$, the original wrapped phase $\phi(x,y)$, is used to generate two separate phase maps: one containing only positive phase gradients $\phi^+(x,y)$ and the other containing only negative phase gradients $\phi^-(x,y)$. Since these phase maps maintain the same size as the original wrapped phase image, all other pixels that do not belong to their respective gradient categories are assigned NaN values. This segmentation is performed using the NaN-masked gradient filter:

$$\phi^+(x,y) = \begin{cases} \phi(x,y), & if\ G_x^+(x,y) \neq NaN; \\ NaN & otherwise \end{cases}$$
$$\phi^-(x,y) = \begin{cases} \phi(x,y), & if\ G_x^-(x,y) \neq NaN; \\ NaN & otherwise \end{cases} \quad (8)$$

where $\phi^+(x,y)$ and $\phi^-(x,y)$ correspond to the segmented positive-gradient and negative-gradient wrapped phase maps, respectively, with non-relevant pixels masked as NaN.

Figures 3(e) and 3(f), and Figures 4(e) and 4(f), respectively, show the segmented wrapped phase maps $\phi^+(x,y)$ and $\phi^-(x,y)$ for Case 1 and Case 2, obtained using a tolerance threshold of $\tau = 0.9\pi$. However, both $\phi^+(x,y)$ and $\phi^-(x,y)$ still contain artefacts near phase-wrapped pixels (values close to $\pm\pi$), particularly manifesting as vertical line patterns. It is noteworthy that if segmentation were instead based on $G_y(x,y)$, these artifacts would tend to appear as horizontal line patterns, due to the corresponding

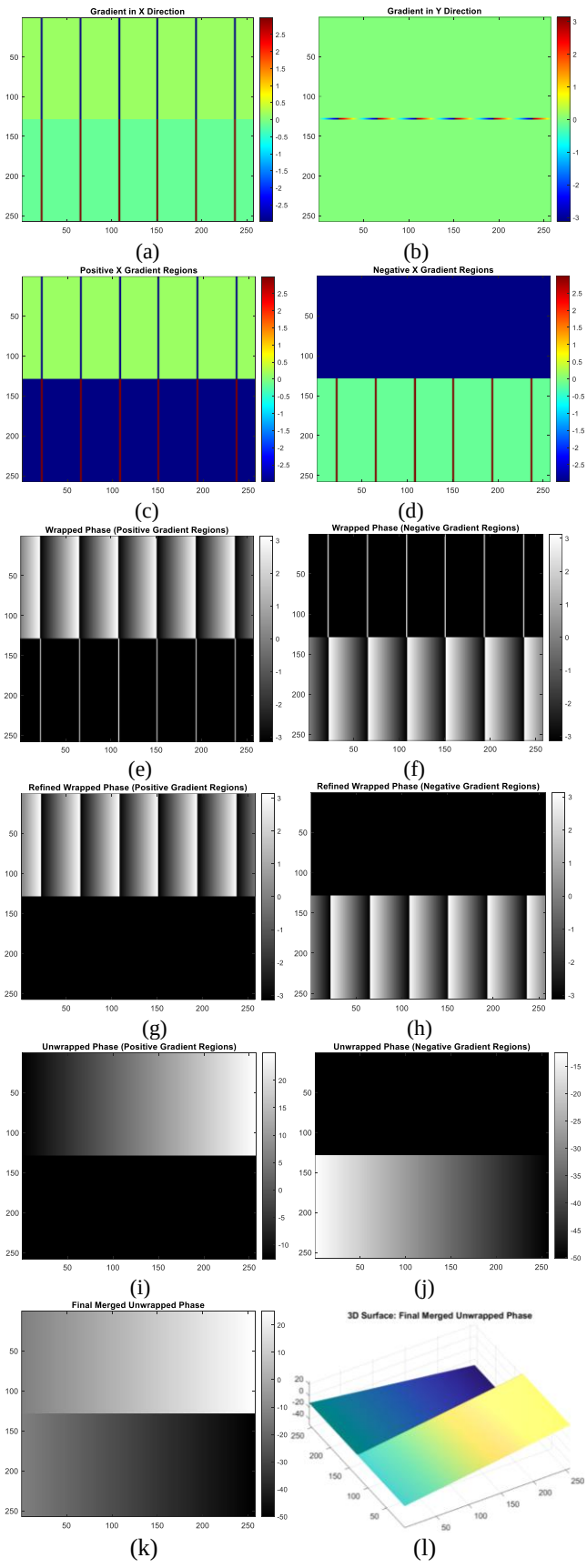

Figure 3. Gradient-based segmentation and phase unwrapping process for the case 1. (a) $G_x(x,y)$ gradient map showing distinct positive and negative regions. (b) $G_y(x,y)$ gradient map, which remains zero throughout the image. (c) and (d) Segmented phase maps based on gradient polarity, where (c) retains only zero or positive gradient pixels, and (d) retains only negative gradient pixels, with all other pixels assigned NaN values. (e) and (f) Segmented wrapped phase maps $\phi^{+}(x,y)$ and $\phi^{-}(x,y)$, respectively, with non-relevant pixels masked as NaN. (g) and (h) Further refinement of segmented wrapped phase maps after artifact suppression near wrapped-phase boundaries. (i) and (j) Independently unwrapped phase maps for positive-gradient and negative-gradient regions, denoted as $\varphi^{+}(x,y)$ and $\varphi^{-}(x,y)$. (k) Final merged unwrapped phase map $\varphi(x,y)$. (l) 3D rendering of the final unwrapped phase surface. Notice that no discontinuity information has been provided to the algorithm at any stage of the process.

directional structure of the phase wrapping in the vertical gradient.

These artifacts arise due to false gradient artifacts at wrapped-phase boundaries, where the left or right neighboring pixel is NaN (or upper/lower for the $G_y(x,y)$ case). To address this, the algorithm identifies phase discontinuities in regions adjacent to NaN pixels and removes spurious phase values by applying the following condition:

If $|\phi^{\pm}(x,y) - \pi| < \tau_a$ *or* $|\phi^{\pm}(x,y) + \pi| < \tau_a$, and at least one neighbour is NaN, then set $\phi^{\pm}(x,y) = \text{NaN}$.

Here, τ_a is the artifact identification threshold, which defines how close a phase value must be to $\pm\pi$ to be classified as an artifact. It is set to $\tau_a = 0.15$, ensuring that only meaningful phase transitions remain while eliminating false artifacts. The results of this further refinement are shown in Figures 3(g) and 3(h), and similarly for the second case in Figures 4(g) and 4(h).

At this stage, both $\phi^{+}(x,y)$ and $\phi^{-}(x,y)$ become significantly simpler to unwrap individually and separately. Following the gradient-based segmentation of the wrapped phase, the phase is unwrapped independently within each segmented region. This approach ensures that phase discontinuities are resolved in a structured manner while preserving spatial consistency. The unwrapped phase maps for the positive-gradient and negative-gradient regions are denoted as:

$$\varphi^{+}(x,y) = \Upsilon[\phi^{+}(x,y)]$$
$$\varphi^{-}(x,y) = \Upsilon[\phi^{-}(x,y)] \quad (9)$$

where $\Upsilon(\cdot)$ represents the unwrapping operator, which restores a continuous phase distribution for each segment independently. The function $\Upsilon(\cdot)$ operates by accumulating phase increments or decrements while resolving 2π ambiguities locally.

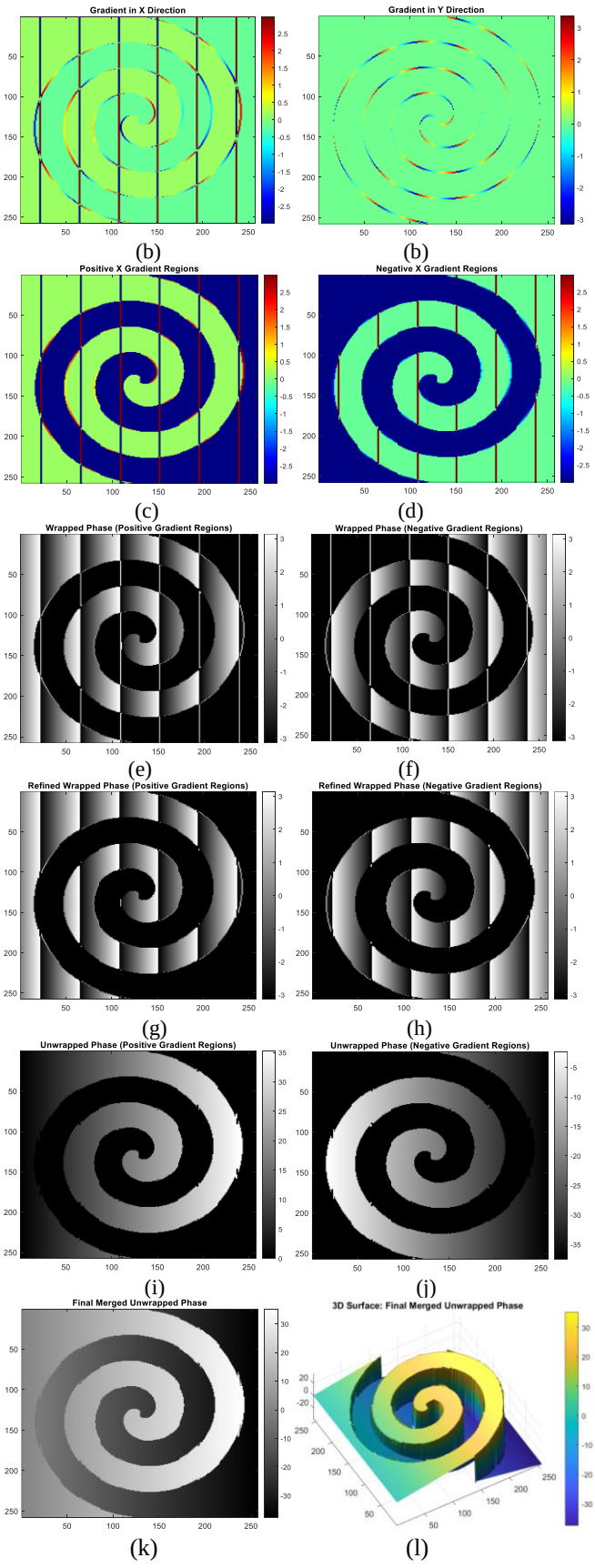

Figure 4. Gradient-based segmentation and phase unwrapping process for the spiral case 2. (a) $G_x(x,y)$ gradient map showing distinct positive and negative regions. (b) $G_y(x,y)$ gradient map, which remains zero throughout the image. (c) and (d) Segmented phase maps based on gradient polarity, where (c) retains only zero or positive gradient pixels, and (d) retains only negative gradient pixels, with all other pixels assigned NaN values. (e) and (f) Segmented wrapped phase maps $\phi^+(x,y)$ and $\phi^-(x,y)$, respectively, with non-relevant pixels masked as NaN. (g) and (h) Further refinement of segmented wrapped phase maps after artifact suppression near wrapped-phase boundaries. (i) and (j) Independently unwrapped phase maps for positive-gradient and negative-gradient regions, denoted as $\varphi^+(x,y)$ and $\varphi^-(x,y)$. (k) Final merged unwrapped phase map $\varphi(x,y)$. (l) 3D rendering of the final unwrapped phase surface. Notice that no discontinuity information has been provided to the algorithm at any stage of the process.

To ensure accurate and robust phase recovery, we adopt a reliability-guided approach [20] for the $\Upsilon(\cdot)$ operator when unwrapping the refined $\phi^+(x,y)$ and $\phi^-(x,y)$.

Figures 3(i) and 3(j) show the unwrapping results of the wrapped phase of $\phi^+(x,y)$ and $\phi^-(x,y)$, respectively, after independent unwrapping. These unwrapped phases are now referred to as: $\varphi^+(x,y)$ and $\varphi^-(x,y)$. Similarly, the corresponding results for the second case are shown in Figures 4(i) and 4(j).

Finally, these two independently unwrapped phase maps, $\varphi^+(x,y)$ and $\varphi^-(x,y)$, are merged to reconstruct the complete unwrapped phase map, denoted as $\varphi(x,y)$. The final unwrapped phase result is shown in Figure 3(k), and the corresponding 3D surface rendering is presented in Figure 3(l). The same results for the second case are shown in Figures 4(k) and 4(l), respectively.

To summarize the proposed algorithm, a simplified flowchart is illustrated in Figure 5, where the diagram concisely outlines the key steps of the method.

It is noteworthy that during the merging process, a few transition-region pixels may remain undefined (NaN), particularly at the border between the two segmented domains. These NaN pixels are considered image artifacts rather than errors in the algorithm itself. To further refine the results, an interpolation step or any reliable approximation method can be applied to replace undefined pixels, ensuring smooth phase continuity across the boundaries of segmented regions.

Nevertheless, it is important to emphasize that the proposed method achieves correct (error-free) unwrapping, except for a small number of border pixels at the interface of the two segments (spirals), which can be further corrected through interpolation or smoothing.

3. Experimental Results

This section presents two experiments that demonstrate the accuracy and robustness of the proposed phase unwrapping

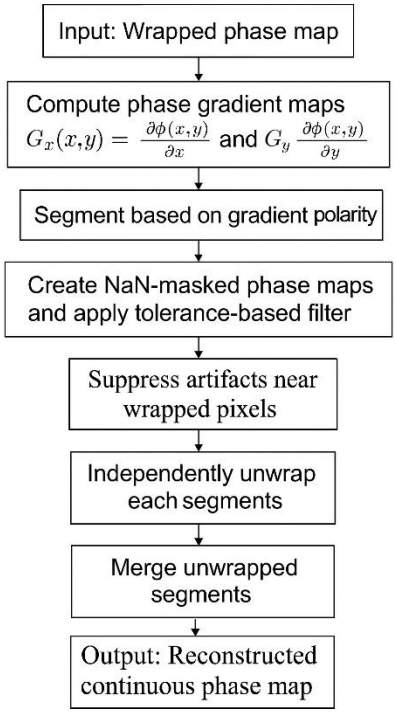

Figure 5. Flow chart of the proposed unwrapping algorithm

algorithm. The first case involves wrapped phase data obtained from an optically measured cylindrical surface with a known discontinuity. The second case uses a simulated interferometric synthetic aperture radar (InSAR) dataset generated from real elevation data. Both cases involve complex phase structures that pose significant challenges for conventional unwrapping methods.

3.1 Wrapped Phase from a Cylindrical Surface with Discontinuity

The wrapped phase map used in this experiment was obtained from a holographic measurement of a test object intentionally designed to contain a sharp discontinuity. The object consisted of a half-cylinder with a diameter of 48 mm, into which a trench of 1 mm depth and 10 mm width was milled to create a step-like surface feature. The object was manufactured with an accuracy of 10 µm.

Imaging was performed using an off-axis digital holography system. The field of view of the setup encompassed a portion of the cylindrical surface, including part of the milled trench. This configuration enabled extraction of the complex amplitude field, from which the wrapped phase map was computed.

The experimentally measured wrapped phase distribution is shown in Figure 6(a). The combination of cylindrical curvature and an abrupt transition in surface height presents a challenging unwrapping scenario. The proposed algorithm was applied without any prior knowledge of the discontinuity. The resulting unwrapped phase map and its corresponding 3D surface reconstruction are presented in Figures 6(b) and 6(c), respectively. As illustrated, the algorithm successfully

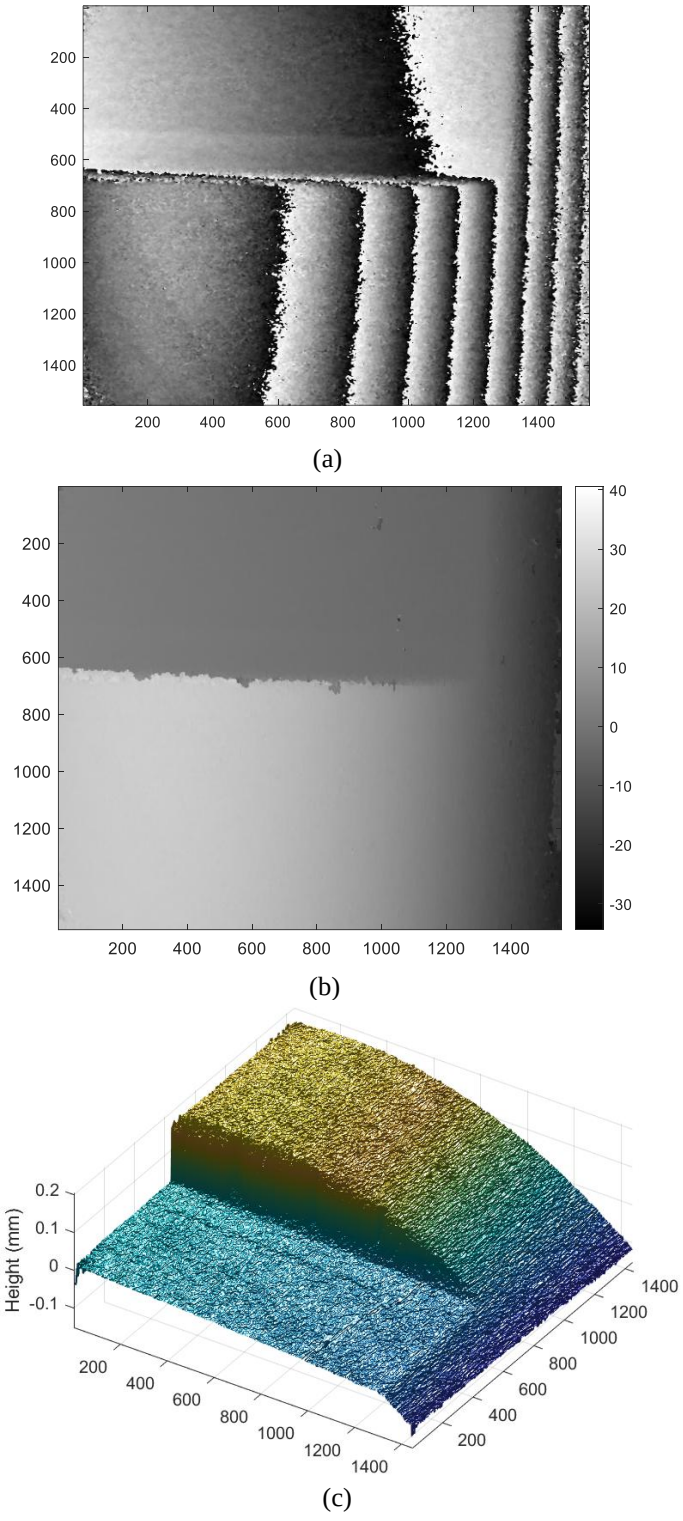

Figure 6. Phase unwrapping of a cylindrical surface with a milled discontinuity. (a) Measured wrapped phase map. (b) Unwrapped phase result. (c) 3D rendering of the reconstructed surface.

recovers the continuous geometry and resolves the depth variation, confirming its robustness for use in optical metrology.

3.1 Simulated InSAR Data Based on Real Terrain

To further evaluate the proposed method, we applied it to a high-fidelity simulated InSAR dataset generated from real topographic data. The wrapped phase map was produced using a digital elevation model (DEM) of mountainous terrain near Longs Peak, Colorado, and provided in [1]. A detailed description of the InSAR simulation model is available in Chapter 3 of [1] and the references therein.

This dataset includes a diverse range of terrain features—such as smooth slopes, steep ridges, and sharp elevation transitions—that introduce phase discontinuities and complex gradient variations. These characteristics, compounded by effects such as layover and shadowing, present significant challenges for unwrapping algorithms.

The proposed method was applied directly to the wrapped phase map without auxiliary information. Figure 7(a) displays the wrapped phase input, while Figure 7(b) shows the corresponding unwrapped result. The reconstructed elevation is rendered in 3D in Figure 7(c). The algorithm successfully resolves both continuous and discontinuous regions, demonstrating strong robustness under realistic InSAR acquisition conditions and simulated geometric distortions.

4. Conclusions

In conclusion, this paper proposes an innovative method that enables fast and accurate phase unwrapping for complex phase maps. By applying gradient polarity-based segmentation and artifact suppression techniques, the refined segmented phase map serves as an optimized input for phase unwrapping algorithms. This structured approach eliminates spurious phase discontinuities, mitigates minor fluctuations, and enhances the reliability of phase estimation. By focusing on localized phase variations where the gradient is consistently positive or negative, the method ensures that phase unwrapping progresses systematically while minimizing error propagation.

Segmentation plays a crucial role in simplifying the phase unwrapping process by dividing the wrapped phase map into independent regions with uniform gradient directions. This not only reduces the complexity of handling abrupt phase transitions but also prevents the influence of reversing or conflicting gradients that could introduce inconsistencies in the final reconstruction. The segmented phase maps provide a structured foundation for unwrapping, allowing seamless unwrapping within each region by preserving consistent phase variations and minimizing discontinuities.

Additionally, incorporating the artifact identification threshold τ_a before unwrapping removes spurious phase values, enhancing accuracy in phase reconstruction.
As a practical consideration, the tolerance threshold τ, used in Eqs. (6) and (7), was empirically tuned based on extensive testing across diverse simulated and experimental datasets. Its selection is also supported by theoretical reasoning: in wrapped phase maps derived from the arctangent function, the phase difference between adjacent pixels should not exceed $\pm 2\pi$. Empirically, we found that values in the range $[0.85\pi, 0.95\pi]$ yield the most consistent and robust result. Lower values tend to overly mask valid gradients, while higher values risk retaining wrap-induced artifacts. The optimal value of τ may vary slightly depending on the

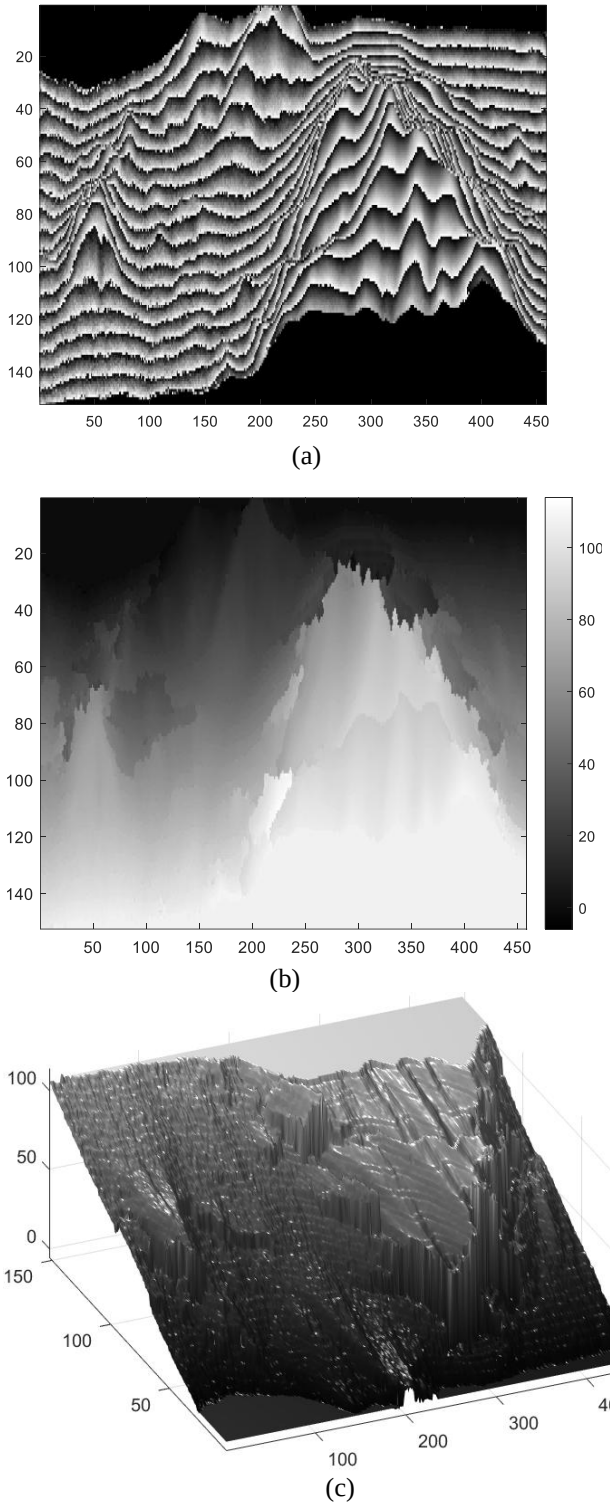

Figure 7. Phase unwrapping of simulated InSAR data. (a) Wrapped phase map generated from real terrain DEM. (b) Unwrapped phase result. (c) 3D surface reconstruction of the recovered elevation.

magnitude of local phase gradients near wrapping boundaries. Similarly, the artifact suppression threshold τ_a , was selected as 0.15 to effectively eliminate spurious discontinuities near ±π, particularly in regions adjacent to NaN pixels. We recommend selecting τ_a within the range [0.14, 0.2] to ensure reliable suppression without compromising valid phase information. These thresholds are essential to maintaining the robustness of segmentation and artifact rejection prior to unwrapping.

A key advantage of adopting a reliability-guided approach in combination with the proposed method is its ability to mitigate common challenges in phase unwrapping, such as error propagation and computational inefficiency. The noncontinuous path strategy within the reliability-guided approach enhances robustness by allowing the algorithm to bypass unreliable or noisy regions, preventing local errors from spreading across the entire phase map. Once segmentation is completed, the unwrapped phase maps from each region are recovered and merged to reconstruct a globally consistent phase distribution. Any potential undefined pixels (NaNs) that may appear at the boundaries of segmented regions are handled through interpolation or smoothing techniques, ensuring that only these NaN values are corrected while preserving the true original phase discontinuities.

Beyond accuracy, the segmentation strategy significantly enhances computational efficiency. By processing independent subregions with a consistent phase gradient polarity, where each segment contains either only positive (or zero) or only negative phase gradients, rather than the entire image at once, the method reduces the problem complexity and size while accelerating the unwrapping process. This is particularly beneficial for large-scale datasets where traditional phase unwrapping methods struggle with global dependencies, causing sequential errors to accumulate. The ability to independently unwrap localized subregions minimizes this issue, allowing for parallel processing and reducing overall computation time.

While the proposed method performs robustly across a wide range of complex phase structures, certain limitations should be acknowledged. Its performance may degrade in cases where the phase map is extremely fragmented, containing a dense distribution of small, disconnected regions with rapidly alternating gradient polarity. In such scenarios, the segmentation process may generate too many isolated segments, particularly around intricate discontinuities. This increases the number of NaN boundaries that require interpolation during the merging phase. Although the method is still capable of recovering the phase under these conditions, the interpolation stage may introduce minor inaccuracies near segment edges, especially where insufficient local context exists for accurate estimation. Additionally, the method can be sensitive to excessive noise levels in the wrapped phase map, which may affect the accuracy of gradient polarity estimation. In such cases, applying slight pre-smoothing prior to computing phase gradients can help stabilize the gradient field and enhance robustness without compromising unwrapping accuracy.

Through simulation and experimental evaluation, it is demonstrated that the proposed method successfully unwraps challenging phase maps, including spiral shear cases, experimental interferometric data, and InSAR datasets, where conventional methods fail. The proposed technique not only provides a robust solution to complex phase unwrapping problems but also establishes a more computationally efficient framework for handling highly wrapped phase structures. With its ability to preserve global phase consistency while addressing local variations, this method represents a significant advancement in interferometric data analysis.

Given the modular structure of the proposed framework, future integration with machine learning techniques holds considerable promise. In particular, adaptive threshold selection, for the tolerance threshold τ and suppression threshold τ_a , could be learned from data to improve robustness across diverse phase conditions. Similarly, advanced deep-learning-based phase reconstruction techniques could enhance the interpolation of undefined (NaN) boundary regions, especially in fragmented or noisy phase maps. Such extensions could further boost both accuracy and real-time applicability in complex environments.

The broader applicability of this approach extends to various fields, including optical metrology, synthetic aperture radar (SAR) imaging, and medical imaging, where accurate and efficient phase unwrapping is critical. By combining structured segmentation, error mitigation, and computational efficiency, the proposed method provides a powerful and scalable solution for modern phase unwrapping challenges.

Funding. The authors acknowledge the financial support of Kempestiftelserna (https://www.kempe.com/) under grant JCSMK24-0156 for this research.

Disclosures. The author declares no conflicts of interest.

Data availability. Data and a ready-to-run MATLAB implementation supporting the results presented in this paper are available in Ref. [26].

References

1. D. C. Ghiglia, "Two-dimentional phase unwrapping: Theory," Algorithms, and Software (1998).
2. C. Zuo, et al., "Temporal phase unwrapping algorithms for fringe projection profilometry: A comparative review," Optics and Lasers in Engineering **85**, 84-103 (2016).
3. K. Wang, et al., "Deep learning spatial phase unwrapping: a comparative review," Advanced Photonics Nexus **1**, 014001-014001 (2022).
4. H. Yu, et al., "Phase unwrapping in InSAR: A review," IEEE Geoscience and Remote Sensing Magazine **7**, 40-58 (2019).

5. D. Khodadad, et al., "Fast and robust automatic calibration for single-shot dual-wavelength digital holography based on speckle displacements," Applied optics **54**, 5003-5010 (2015).
6. X. Su and W. Chen, "Reliability-guided phase unwrapping algorithm: a review," Optics and Lasers in Engineering **42**, 245-261 (2004).
7. D. Khodadad, et al., "Temperature Sensing in Space and Transparent Media: Advancements in Off-Axis Digital Holography and the Temperature Coefficient of Refractive Index," Applied Sciences **13**, 8423 (2023).
8. C. Wagner, et al., "Direct shape measurement by digital wavefront reconstruction and multi-wavelength contouring," Optical Engineering **39**, 79-85 (2000).
9. C. J. Mann, et al., "Quantitative phase imaging by three-wavelength digital holography," Opt. Express **16**, 9753-9764 (2008).
10. B. Tayebi, et al., "Reduced-phase dual-illumination interferometer for measuring large stepped objects," Optics letters **39**, 5740-5743 (2014).
11. D. Khodadad, "Combined Reduced Phase Dual-Directional Illumination Digital Holography and Speckle Displacements for Shape Measurement," International Journal of Optics **2019**, 4906109 (2019).
12. B. Tayebi, et al., "Large step-phase measurement by a reduced-phase triple-illumination interferometer," Opt. Express **23**, 11264-11271 (2015).
13. T. Li, et al., "Enlarged range of measurement method with strong noise resistance for dual-wavelength digital holography," Optics Letters **46**, 4694-4697 (2021).
14. M. Shan, et al., "Surpassing the differential synthetic wavelength of dual-wavelength digital holography by optimizing the search for an unwrapping coefficient," Optics Letters **50**, 2990-2993 (2025).
15. H. Sabahno, et al., "Adaptive resolution in speckle displacement measurement using optimized grid-based phase correlation and statistical refinement," Sensing and Bio-Sensing Research **48**, 100790 (2025).
16. P. Bergström, et al., "Dual-wavelength digital holography: single-shot shape evaluation using speckle displacements and regularization," Applied Optics **53**, 123-131 (2014).
17. Y. Lu, et al., "Phase unwrapping based on branch cut placing and reliability ordering," Optical Engineering **44**, 055601-055601-055609 (2005).
18. L. Ying, "Phase unwrapping," Wiley Encyclopedia of Biomedical Engineering (2006).
19. K. Itho, "Analysis of the phase unwrapping problem," Appl. Opt. **21**, 2470 (1982).
20. M. A. Herráez, et al., "Fast two-dimensional phase-unwrapping algorithm based on sorting by reliability following a noncontinuous path," Applied Optics **41**, 7437-7444 (2002).
21. J. M. Bioucas-Dias and G. Valadao, "Phase unwrapping via graph cuts," IEEE Transactions on Image processing **16**, 698-709 (2007).
22. Z. Zhao, et al., "Robust 2D phase unwrapping algorithm based on the transport of intensity equation," Measurement Science and Technology **30**, 015201 (2018).
23. T. J. Flynn, "Two-dimensional phase unwrapping with minimum weighted discontinuity," J. Opt. Soc. Am. A **14**, 2692-2701 (1997).
24. D. C. Ghiglia and L. A. Romero, "Minimum Lp-norm two-dimensional phase unwrapping," J. Opt. Soc. Am. A **13**, 1999-2013 (1996).
25. M. Gdeisat and F. Lilley, "Two-dimensional phase unwrapping problem," ljmu. ac. uk **1**, 1-32 (2016).
26. D. Khodadad, "MATLAB Code and Example Data for Fast and Accurate Phase Unwrapping of Complex Phase Maps," (https://doi.org/10.6084/m9.figshare.29571782, 2025).

Citation: Davood Khodadad, "Fast and accurate phase unwrapping for complex phase maps," Appl. Opt. 64, 6910-6917 (2025) https://doi.org/10.1364/AO.567228

View publication stats